

Vignetting effect in Fourier ptychographic microscopy

An Pan^{a,b}, Chao Zuo^{c,*}, Yuege Xie^d, Ming Lei^a, Baoli Yao^{a,*}

^a State Key Laboratory of Transient Optics and Photonics, Xi'an Institute of Optics and Precision Mechanics, Chinese Academy of Sciences, Xi'an 710119, China

^b University of Chinese Academy of Sciences, Beijing 100049, China

^c Smart Computational Imaging (SCI) Laboratory, Nanjing University of Science and Technology, Nanjing 210094, China

^d Institute for Computational Engineering and Sciences, University of Texas at Austin, TX 78712 USA

ARTICLE INFO

Keywords:

Vignetting
Fourier ptychographic microscopy
Coherent imaging system
Fourier optics and signal processing

ABSTRACT

In the usual model of Fourier ptychographic microscopy (FPM), the coherent microscopic system is approximated by being taken as linear space-invariant (LSI) with transfer function determined by a complex pupil function of the objective. However, in real experimental conditions, several unexpected “semi-bright and semi-dark” images with strong vignetting effect can be observed when the sample is illuminated by the LEDs within the “transition zone” between bright field and dark field. These imperfect images, apparently, are not coincident with the LSI model and could deteriorate the reconstruction quality severely. Herein, we investigate the cause and the impact of model misfit based on ray-based and rigorous wave optics-based analysis. Our analysis shows that for a practical FPM microscope with a low magnification objective and a large field-of-view (FOV), the LSI model breaks down as a result of diffraction at other stops or apertures associated with different lens elements. A modified version of the linear space-variant (LSV) model is derived for quantitative analysis. The spectrum of the object will be modulated unexpectedly by a quadratic phase term relatively if assuming the shape of pupil function is invariable. Two countermeasures are also presented and experimentally verified to bypass or alleviate the vignetting-induced reconstruction artifacts. An adaptive update order and initial guess strategy is proposed and demonstrated for better reconstructions. Our work gives a deeper insight into the vignetting effect on wide-FOV imaging and provides a useful guide for easily achieving improved FPM reconstructions that bypass the adverse effect.

1. Introduction

Fourier ptychographic microscopy (FPM) [1–9] is a fast-growing computational imaging technique with high resolution (HR), wide field-of-view (FOV), and quantitative phase recovery, which shares its root with conventional ptychography [10,11], synthetic aperture imaging [12,13], and structured-illumination imaging [14,15]. Different from the traditional bright-field (incoherent) microscope based on the Köhler illumination, FPM is a coherent imaging technique by replacing the condenser of traditional microscope with a LED array. Instead of starting with HR and stitching together a larger FOV, FPM uses low numerical aperture (NA) objective to take advantage of its innate large FOV and stitches together low resolution (LR) images in Fourier space to recover HR. For a periodically structured sample illuminated by a coherent monochromatic plane wave propagating perpendicular to the sample surface, the classical Abbe's theory of image formation states that if, and only if, the first order diffraction spots in the Fourier plane images can be collected by the microscope objective lens, then a periodic image will be formed in the real plane of the microscope. However, if the radiation emitted by the source of illumination is not a plane wave im-

pinging perpendicularly to the sample, then the Abbe's theory statement of image formation should be rephrased as follows: if a fraction of the first order diffraction features can be captured by the microscope objective lens, then the periodic structure of the object will be visible in the image [1–3]. Therefore, the smallest resolvable object detail of FPM is $\lambda / (NA_{\text{illu}} + NA_{\text{obj}})$, since higher NA_{illu} can be scattered into the objective lens in the coherent case, where λ is the wavelength, NA_{illu} and NA_{obj} are the NA of illumination and objective lens respectively. In fact, this formula can be also generalized to the incoherent case where the NA_{illu} is equal to the NA_{obj} . Due to its flexible setup, promising performance without mechanical scanning and interferometric measurements, FPM has wide applications in the digital pathology [16], whole slide imaging [17], and fluorescence imaging [18,19].

Generally, the coherent microscopic system, for example, the FPM, is simplified to a linear space-invariant (LSI) 4-f imaging system with coherent transfer function (CTF) determined by a complex pupil function of the objective, and a simple convolution operation describing the object-image relationship is applied [1–3,20]. In real experimental conditions, however, there are three phenomena that are not coincident with the LSI model of FPM. First, the simulations are incon-

* Corresponding authors.

E-mail addresses: surpasszuo@163.com (Chao Zuo), yaobl@opt.ac.cn (Baoli Yao).

sistent with the experimental observations. Several unexpected “semi-bright and semi-dark” imperfect images can be easily observed when the sample is illuminated by the LEDs within the “transition zone” between bright field (BF) and dark field (DF). These imperfect images, apparently, are not coincident with the LSI model where there are only BF or DF images. Second, the resolution with the adjacent tilted incidence is varied with the space compared with the normal incidence. While the cut-off frequency along one axis is invariable theoretically in the LSI model with the adjacent tilted incidence, which means the resolution with the adjacent tilted incidence should not be varied along the relative axis. And similar phenomenon was also observed by Horstmeyer et al. [21], the resolution will decrease from the center to the edge of FOV. Third, these imperfect images could deteriorate the reconstructions of FPM severely without block processing. All these phenomena indicate that the model may not be ideally space-invariant but space-variant. In this paper, we investigate the causes and the impact of model misfit based on ray-based and rigorous wave optics-based analysis. Our analysis shows that for a practical FPM microscope with a low magnification objective and a large FOV, the LSI model is destroyed by diffraction at other stops or apertures associated with different lens elements to a large extent, termed vignetting. The pupil function will not always be illuminated fully and is varied with the space. Generally, it is easy to understand the vignetting from the perspective of the geometrical optics. But how the vignetting affects the image quality and reconstructions from the perspective of wave optics is unexplored until now. A modified version of the linear space-variant (LSV) model is derived for quantitative analysis. The spectrum of the object will be modulated unexpectedly by a quadratic phase term relatively if assuming the shape of pupil function is invariable. Different from other system errors, e.g., aberrations [22], LED intensity fluctuations [23], positional misalignment [24,25], and noise [26], which may generate similar artifacts, the vignetting degrades the reconstructions with completely different physical mechanism and cannot be solved with state-of-the-art calibration methods [22–30].

To this end, two simple countermeasures are proposed to bypass or alleviate the vignetting-induced reconstruction artifacts. The first strategy is to divide the FOV into smaller patches, making the space-variance to local space-invariance. The smaller the patch is, the more reasonable the LSI approximation is. Though the FPM is usually implemented based on block processing, the purpose is to save the memory and process data in parallel [1–3]. In other words, we found that the block processing is not an optional strategy but a policy that must be obeyed. However, only block processing is not enough, because some of small patches may still contain imperfect or incompatible information compared with the ideal (simulated) segments, which may lead to erroneous or unrealistic values in the error matrix and make the algorithm strongly oscillatory or even divergent. Thus, involving these imperfect segments cannot improve the reconstruction quality but will introduce strong artifacts. Based on this idea, the second strategy is to omit those imperfect segments to maintain the consistency of FPM dataset based on automatic outlier removal. The performance has been experimentally verified both with USAF targets and biological samples and been verified with the open data of Tian et al. [31] for cross validation. For those patches near the edge of FOV, the normal incidence light is not always the light from the center LED. An adaptive update order and initial guess strategy is proposed and demonstrated for better reconstructions. Our work gives a deeper insight into the vignetting effect on wide-FOV imaging and provides a useful guide for easily achieving improved FPM reconstructions that bypass the adverse effect.

2. Basic principle of FPM (LSI model)

The schematic and experimental configurations of FPM are shown in Fig. 1. A 32×32 programmable R/G/B LED array (Adafruit, 4 mm spacing, controlled by an Arduino) is placed at 68.4 mm above the sample, while 15×15 center LED elements are lighted up sequentially

for the data acquisition process. The height is random chosen for illustration. The red, green and blue LEDs have a dominant narrow peak at the wavelength of 631 nm, 516 nm and 465 nm within 20 nm bandwidth respectively, while only the red LEDs are used to provide angle-varied illuminations in this experiment. A compact inverted microscope is used as shown in Fig. 1(a2) with light path diagram, which can be further combined with the fluorescence imaging easily [32]. All the data are captured by a $4\times/0.1\text{NA}$ apochromatic objective and a 16-bits sCMOS camera (Neo 5.5, Andor, 2160×2560 pixels, $6.5 \mu\text{m}$ pixel pitch). Though the LED light is partial coherent indeed, the existing algorithms of FPM regard the raw data as coherent case due to two reasons. One is that the bandwidth of our LEDs is within 20 nm, which is very narrow and meets the quasi-monochromatic approximation $\Delta\lambda \ll \lambda$ [20]. The other reason is that the LED element is very small ($3 \text{ mm} \times 3 \text{ mm}$), namely the light-emitting area is small. When we divide the FOV into many small patches, for example, 200×200 pixels in our experiments, the coherence area [20] defined by $d_c \approx h\lambda/b$ is fulfilled, where d_c is the side length of the coherence area, h is the distance between the LED element and the sample, and b is side length of the LED light-emitting area.

In FPM, the problem can be deemed to be a non-convex optimization to recover the HR complex field of the object from a number of LR intensity measurements with different illumination angles. For a finite set of illumination vectors $k_{m,n}$, each intensity image is denoted by [1–3]:

$$I_i(r) = \left| \mathcal{F}_{[O(k-k_i)P(k)]}(r) \right|^2 \quad (1)$$

where $r = (x, y)$ denotes the lateral coordinates in the sample plane, $k = (k_x, k_y)$ denotes the lateral coordinates in the Fourier domain, $k_i = (k_{x,i}, k_{y,i})$ is the spatial frequency of the local plane wave emitted by each LED; $P(k)$ is the pupil function, $O(k-k_i)$ represents the exit wave at the pupil plane, and subscript i is the sequence number of LR images; $\mathcal{F}\{\cdot\}$ is the 2D Fourier transform, which can be defined by

$$\mathcal{F}_{[g]}(x, y) = \iint g(k_x, k_y) \exp[-j(xk_x + yk_y)] dk_x dk_y \quad (2)$$

where $g(\cdot)$ is a virtual function, j is the imaginary unit, and the original 2π in the Fourier transform is contained in the k space. To retrieve the Fourier spectrum of the object function $O(k)$, the well-known solution to FPM uses the incremental gradient approach [26,27], which can be derived by formulating FPM as the following optimization problem to minimize the differences of the amplitude between the simulated patterns and captured images.

$$\min_{O(k)} \varepsilon = \min_{O(k)} \sum_i \sum_r \left| \sqrt{I_i(r)} - \left| \mathcal{F}_{[O(k-k_i)P(k)]}(r) \right| \right|^2 \quad (3)$$

The algorithm uses only one intensity measurement for each update and after all the measurements are utilized once can be regarded as a single iterative process. The whole iterative process is repeated for several times until the error matrix convergences. The error matrix can be defined as [26]

$$\varepsilon = \sum_i \left\| \sqrt{I_i} - |\mathcal{F}P_iO| \right\|^2 \quad (4)$$

which quantifies the overall difference between the estimated intensities and the experimentally captured ones. It is not difficult to understand that a reasonably ‘good’ estimate of O should create a sparse error matrix with values as small as possible.

3. Vignetting effect in a practical wide-field microscopic system

There are three phenomena that are not coincident with the usual LSI model of FPM. First, the simulations are inconsistent with the experiments. The LR images are simulated according to the LSI model as shown in Fig. 2(b) with either BF or DF images. However, in real experimental conditions, several unexpected “semi-bright and semi-dark” images with strong vignetting effect can be easily observed when the

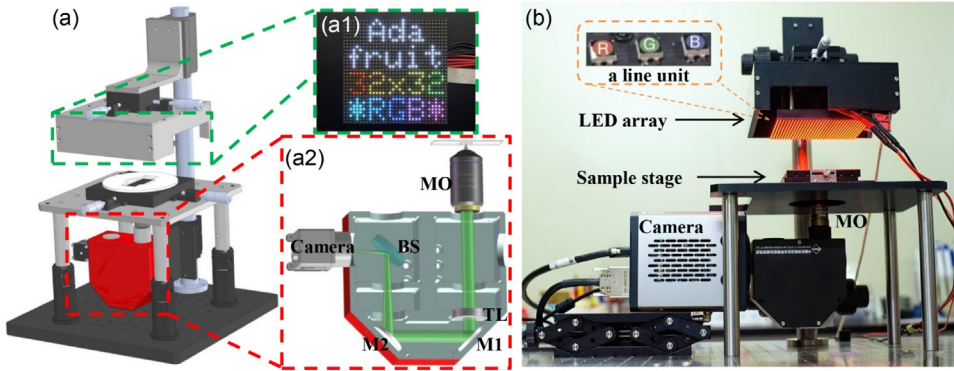


Fig. 1. (a) Schematic of traditional FP platform with LED board. (a1) A 32×32 programmable R/G/B LED matrix. (a2) The enlargement of a compact inverted microscope with light path diagram. MO: microscope objective; TL: tube lens; M1 and M2: mirrors; BS: beam splitter. (b) Photographs of the corresponding optical setups.

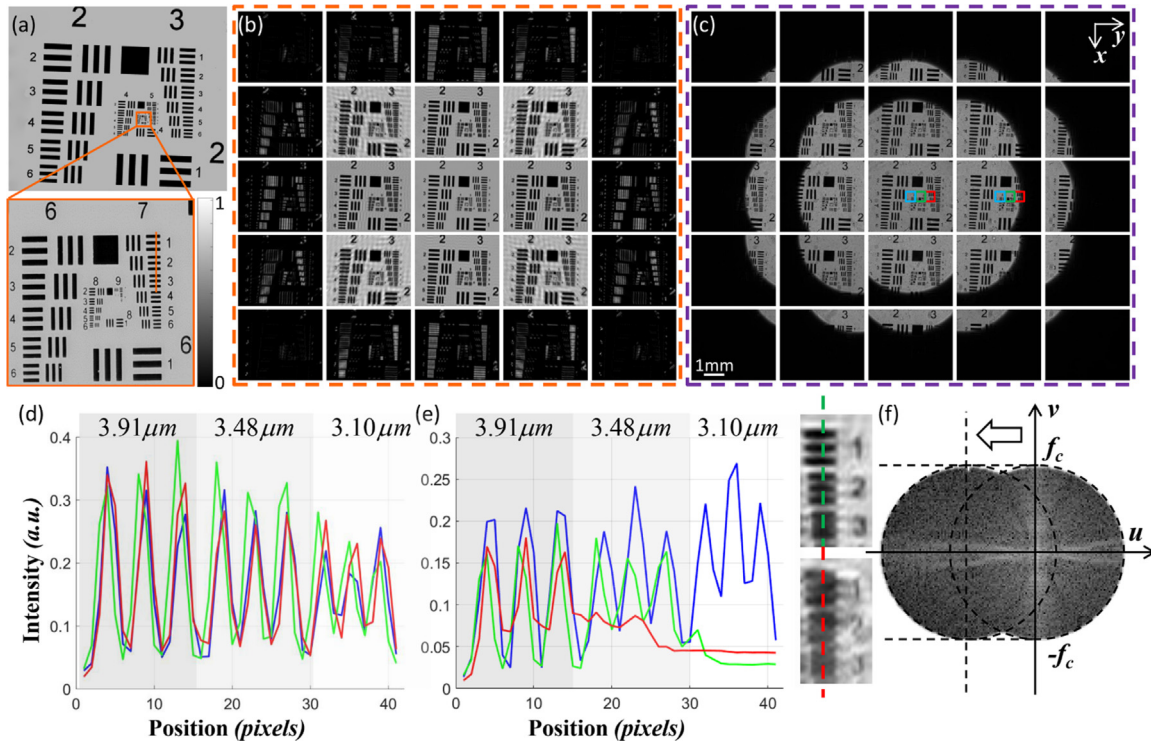


Fig. 2. (a) Ground truth for simulations captured by an $20\times/0.45\text{NA}$ objective and its close-up. (b) Twenty five center images captured by an $4\times/0.1\text{NA}$ objective with simulations and experimental observations respectively. (c) The center of USAF target is placed at red, green and blue rectangular regions in Fig. 2(c), respectively and their corresponding profiles of element 1–3, group 7 ($3.10\text{--}3.91\ \mu\text{m}$) with normal incidence and the adjacent tilted incidence, respectively. (d) The theoretical passband of normal incidence and the adjacent tilted incidence.

sample is illuminated by the LEDs within the “transition zone” between BF and DF, as shown in Fig. 2(c).

Second, the center of USAF target is placed at red, green and blue rectangular regions respectively as shown in Fig. 2(c) and their corresponding profiles of element 1–3, group 7 ($3.10\text{--}3.91\ \mu\text{m}$) with normal incidence and the adjacent tilted incidence respectively are shown in Fig. 2(d) and (e). The resolution with the adjacent tilted incidence is varied with the space compared with the normal incidence. While the cut-off frequency along v -axis is invariable theoretically in the LSI model with the adjacent tilted incidence, which means the resolution with the adjacent tilted incidence should not be varied along the x -axis. And similar phenomenon was also found by Horstmeyer et al. [21], the resolution will decrease from the center to the edge of FOV.

Third, with the captured datasets in experiments, the reconstructions cannot be implemented without block processing (direct full-FOV reconstruction) due to the misfit of the imaging model. The contrast of intensity and phase decreases and there will be obvious wrinkles especially at the edge of FOV as shown in the green and purple regions of Fig. 3(a)

and (b). The close-ups are shown in Fig. 3(d1)–(d4). The spectrum is enlarged, as shown in the red arrow of Fig. 3(c).

4. Linear space-variant (LSV) model

By inspecting the ray-based schematics shown in Fig. 4(a), it is not difficult to understand the causes of the above-mentioned phenomena. In the conventional analysis of 4-f imaging systems with coherent illumination, it is generally assumed that even though an imaging system may consist of several optical elements, respectively with its own aperture, these elements are often lumped together in a single “black box,” and only the exit or the entrance pupil is used to describe the effects of diffraction [20,33,34]. In the paraxial regime, this simplified analysis indeed results in a LSI model. However, if the objective L_1 is not infinite in extent, the wave leaving L_1 is subject to the effect of diffraction by the lens aperture itself. Often the diameter of tube lens L_2 is greater than objective L_1 , L_2 can be infinite to some extent, and vignetting can be introduced by the finite aperture of the objective L_1 . Point source PS_{VL} (pink

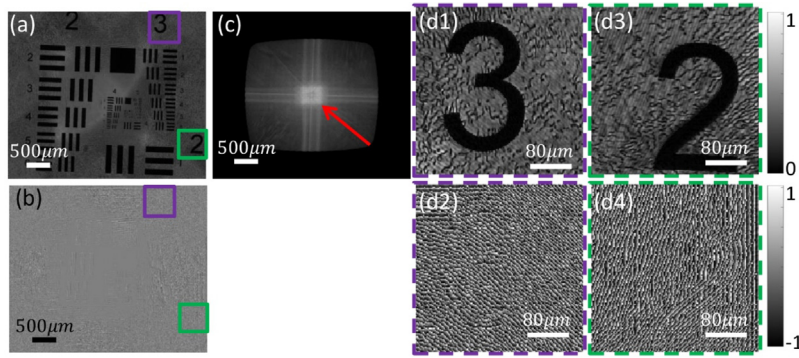


Fig. 3. Reconstructions of FPM without block processing and its close-ups (200 × 200 pixels) in experiments. (a) Intensity; (b) Phase; (c) Fourier spectrum; (d1–d4) The close-ups of purple and green regions in Fig. 3(a) and Fig. 3(b), respectively.

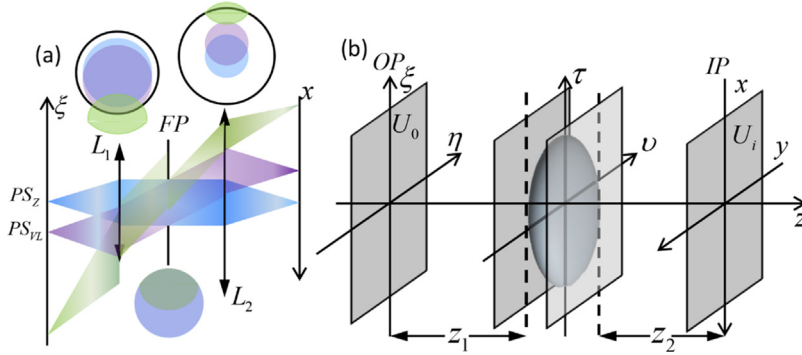


Fig. 4. (a) Example of vignetting in a simplified 4-f imaging system for off-axis point (pink light) and even farther off-axis point (green light) from the ray-based analysis; FP, Fourier plane; L_1 , the objective; L_2 , tube lens; PS, point source. (b) A single lens system for illustration from the wave optics-based analysis; OP, object plane; IP, image plane.

light) marks the onset of vignetting in the geometrical optics regime, and we use the subscript VL to refer to this point as the vignetting limit. For even farther off-axis point, for example, the green light in Fig. 4(a), the aperture delimiting L_1 eliminates part of the light and the aperture in Fourier plane is thus no longer fully illuminated. With vignetting, the region of the Fourier plane aperture that is no longer illuminated cannot contribute to the distribution in the image plane. The consequences of this diffraction depend on the location of the point source, and thus the imaging operation is space variant and must be described not by a convolution integral but rather by a more general superposition integral.

From the perspective of wave optics with coherent illumination as shown in Fig. 4(b) for illustration, we simplify the system to a single lens system with focal length f , the field U_i can always be represented as superposition integral as follows, since the wave propagation is linear. Note that Fig. 4(a) and (b) are two separate systems and the coordinate system has been rotated symmetrically.

$$U_i(x, y) = \iint h(x, y; \xi, \eta) U_0(\xi, \eta) d\xi d\eta \quad (5)$$

where $h(\bullet)$ is the point spread function (PSF) of this system. In order to get the PSF, let the object function be a δ function at the (ξ, η) plane. Then with the Fresnel transform, the optical field of image plane can be given by [20]

$$h(x, y; \xi, \eta) = \exp \left[j \frac{k}{2z_2} (x^2 + y^2) \right] \exp \left[j \frac{k}{2z_1} (\xi^2 + \eta^2) \right] \times \iint P(\tau, v) \exp \left[j \frac{k}{2} \left(\frac{1}{z_1} + \frac{1}{z_2} - \frac{1}{f} \right) (\tau^2 + v^2) \right] \exp \left\{ -jk \left[\left(\frac{\xi}{z_1} + \frac{x}{z_2} \right) \tau + \left(\frac{\eta}{z_1} + \frac{y}{z_2} \right) v \right] \right\} d\tau dv \quad (6)$$

where $P(\tau, v)$ is the pupil function of the lens, and the constant term is ignored. There are three quadratic phase factors. The term in integral can be easily eliminated if the equation $1/z_1 + 1/z_2 = 1/f$ holds, which is the precondition for imaging, where z_1, z_2 are the object distance and image distance respectively. The other two terms are outside the integral. The one which is associated with the image plane can be ignored if we only consider the intensity. The residual term, which is associated with the object plane, is really intractable since it contains the integral term with

respect to the (ξ, η) in Eq. (5) and will have a significant impact to the final results. Goodman et al. [20,35] have discussed and proposed the approximate condition to compensate or ignore it in detail. And consequently, the generally used and simplified formula of PSF is well known as follows, which is the Fourier transform of pupil function.

$$h_p(x, y; \xi, \eta) \approx \iint P(\tau, v) \exp \left\{ -j \frac{2\pi}{\lambda z_2} [(x - M\xi)\tau + (y - M\eta)v] \right\} d\tau dv \quad (7)$$

where M is the magnification, which is equal to $-z_2/z_1$, and the constant term is ignored. The simplified PSF is space-invariant and the observation field can really be calculated with Eq. (1). However, the approximate condition of the term associated with the object plane cannot be satisfied in FPM, since the objective cannot be deemed to be infinite in extent again. Thus the rigorous PSF is

$$h_c(x, y; \xi, \eta) = \exp \left[j \frac{k}{2z_1} (\xi^2 + \eta^2) \right] h_p(x, y) \quad (8)$$

In Goodman's book [20], it only gives the simplified formula and does not discuss the situation further if the approximate condition is not satisfied. Here we take the Eq. (8) into Eq. (5) and let $\xi' = M\xi, \eta' = M\eta$ and unexpectedly derive our LSV model as follows.

$$U_i(x, y) = \iint \frac{1}{|M|} U_0 \left(\frac{\xi'}{M}, \frac{\eta'}{M} \right) \exp \left[\frac{jk}{2z_1} \left(\frac{\xi'^2 + \eta'^2}{M^2} \right) \right] \quad (9)$$

$$h_p(x - \xi', y - \eta') d\xi' d\eta' \quad (9)$$

And we rewrite it to

$$U_i(x, y) = \mathcal{F}^{-1} \left\{ \mathcal{F} \left\{ \frac{1}{|M|} U_0 \left(\frac{x}{M}, \frac{y}{M} \right) \exp \left[\frac{jk}{2z_1} \left(\frac{x^2 + y^2}{M^2} \right) \right] \right\} P(-\lambda z_2 f_\tau, -\lambda z_2 f_v) \right\} \quad (10)$$

where $f_\tau = \tau/\lambda z_2, f_v = v/\lambda z_2$, and the constant term is ignored. The spectrum of object function will be modulated unexpectedly by a quadratic phase term if assuming the shape of pupil function is invariable according to the quantitative expression of Eq. (10).

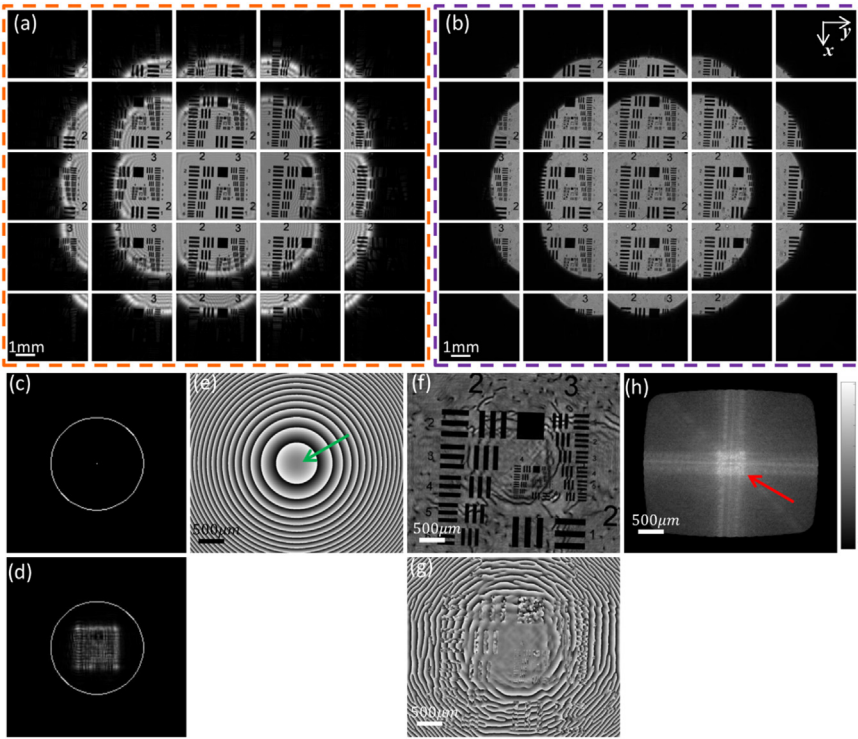


Fig. 5. (a) Simulations with our LSV model. (b) Experimental observations. (c,d) Fourier spectrum and cut-off frequency of LSI model and LSV model with the normal incidence respectively. (e) The phase mask for modulation. (f,g,h) The recovered intensity, phase, and Fourier spectrum in simulations with the raw data of LSV model respectively.

In simulation, we set M is $-4\times$, NA is 0.1 and found f is equal to 50 mm while z_1 is equal to $(|M| + 1)f/|M|$ and z_2 is equal to $|M|z_1$ respectively. Fig. 5(a) shows the simulations with our LSV models, which closely match the experimental observations as shown in Fig. 5(b) (i.e. Fig. 2(c)). And with the simulated data, the reconstructed intensity, phase, and Fourier spectrum without block processing are shown in Fig. 5(f)–(h), respectively, which nearly reproduce the results shown in Fig. 3. There will be obvious phase ramp and wrinkle at the edge of FOV and the spectrum has also been enlarged as shown in red arrow in Fig. 5(h). Generally, in the LSI model, object spectrum demonstrates a punctual central frequency at origin, as shown in Fig. 5(c). If the cut-off frequency contains the spike frequency, the LR image is a BF image, otherwise it is a DF image. However, in LSV model the object is modulated unexpectedly by a quadratic phase term shown in Fig. 5(e), which broadened the spectrum into a square shape, as shown in Fig. 5(d). Note that similar problems are also encountered in digital holographic microscopy [36]. That is the reason that why the recovered spectrum in Fig. 3(c) and Fig. 5(h) was enlarged. Only if the FOV is sufficiently small and is in the central region (indicated by the green arrow) of the quadratic phase distribution shown in Fig. 5(e), the LSV model can be degenerate into the LSI model.

Compared with the other four known system errors in FPM, the model of Eq. (1) will be modified to

$$I_i(r) = w_i \left| \mathcal{F}[O(k-k_i - \Delta k_i)P(k)e^{i\phi}](r) \right|^2 + I_{n,i} \quad (11)$$

where the weight factor w_i is introduced by the LED intensity fluctuations [23,25], the phase term $e^{i\phi}$ is introduced by the aberrations [22], which is included in the pupil function, the intensity term $I_{n,i}$ is introduced by the noise [26,29]. And the positional misalignment [24,25] would make the estimation of k_i not precise and introduce the term Δk_i . Our LSV model of Eq. (10) for vignetting would degrade the reconstructions with different physical mechanism apparently, while other system errors are under the case of LSI model and those state-of-the-art calibration methods cannot be used to solve the error from vignetting effect.

5. Countermeasures for the LSI-induced artifacts

5.1. Local linear space-invariance approximation

The LSV model can well explain the phenomena described in Section 3, but it cannot fully match the realistic conditions since i) There are apparent Gibb's phenomena [37] at the edge of clear aperture shown in Fig. 5(a); ii) An objective is generally a complex set of optics, which cannot be precisely modelled by a single-lens system; iii) Uncertain aberrations, stray lights, noise and the partial coherence of the LED light source cannot be evaluated precisely either. All these factors will smooth the contour of transition regions. But except for these edge parts, the internal BF and external DF are well coincident with the observations. It should also be noticed that these abnormal images are quite difficult to be precisely characterized by merely improving the LSI imaging model because too many factors, e.g. aberrations, stray lights, noise, and partial coherence of the illumination, are involved in the image formation. Therefore, directly using the LSV model for the reconstructions of FPM is difficult and even impossible. Besides, the optimization problem might be significantly complicated due to the changes of cost function and gradients and other parameters for different objective lens. Otherwise, we must measure the space-varied CTF precisely.

So the first strategy we propose is to divide the FOV into smaller patches, making the space-variance approximate to local space-invariance. The smaller the patch is, the more reasonable the LSI approximation is. The reconstructions of the USAF target of the blue and red regions in Fig. 2(c) are presented in Fig. 6. With block processing, the segments of central blue region of Fig. 2(c) as shown in Fig. 6(c), which are matched with the LSI model, since the center region can be deemed to be space-invariant illustrated in Fig. 5(e). And the reconstructions are improved compared with the results without block processing in Fig. 3. However, only block processing is not enough, because the small patches may still contain several imperfect or incompatible segments compared with the simulated segments, especially those patches that are not the center of the FOV. For illustrations, the segments of the red region in Fig. 2(c) as shown in Fig. 6(d) are not matched with

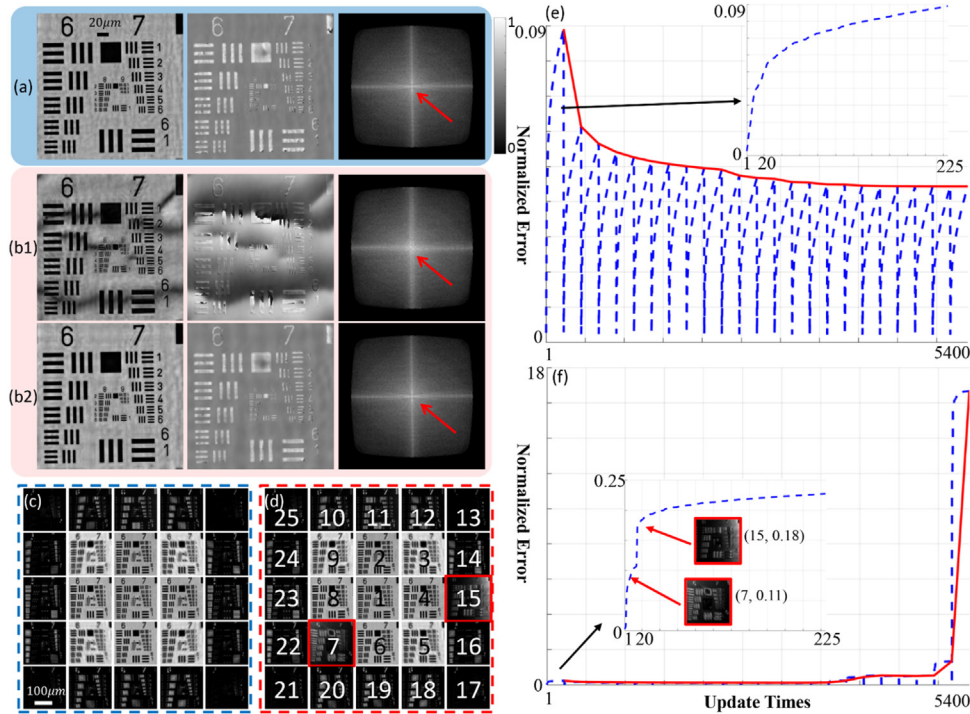


Fig. 6. (a,b1,b2) The reconstructions of USAF target placed at the blue and red region (150×150 pixels) in Fig. 2(c) with block processing respectively; They share the same scale bar of $20 \mu\text{m}$. (c, d) The corresponding segments of Figs. 6(a) and (b), respectively and automatically selected segments to be omitted (red boxes). Sequence number, update order; They share the same scale bar of $100 \mu\text{m}$. (e,f) The error matrix of Fig. 6(a) and (b) respectively. Red line, error curves with iterations; blue line, error curves with sub-iterations for each segment. A full iteration contains 255 updates (sub-iterations).

the ideal model. And there will obvious artifacts in its reconstructions as shown in Fig. 6(b1) and the spectrum (red arrow) is still a little enlarged even being divided into small patches compared with Fig. 6(a), although they are much better than the results without block processing as shown in Fig. 3(c). The update order is fixed for all the results unless otherwise noted as shown in the sequence numbers of Fig. 6(d). The error matrix is used to evaluate the reconstruction quality as shown in Fig. 6(e) and (f). All the error curves have been normalized by dividing the sum of raw segments. One full iteration contains 255 updates (sub-iterations) since we capture 255 LR images. The red line shows the error with iterations, while the blue line shows the error with sub-iterations for each segment. The FPM algorithm converges within 24 iterations, i.e. 5400 updates. Ideally, each image should contribute a small portion of increment to the error matrix during iterations. However, the imperfect or incompatible segments (red boxes in Fig. 6(d)) lead to several abnormal jumps of the error matrix for every iteration if we compared the subgraph of Fig. 6(e) with Fig. 6(f). The error in the subgraph of Fig. 6(f) is 3 times higher than the ideal situations in Fig. 6(e) after the first iteration and will be enlarged with more iterations (note the significant difference (0.09 and 18) of the maximum y-coordinate between Fig. 6(e) and (f)). These two imperfect or incompatible segments make the algorithm strongly oscillatory and finally divergent, as shown in Fig. 6(e). The reconstruction result shown in Fig. 6(b1) suggests that involving these imperfect segments cannot improve the reconstruction quality but may introduce strong wrinkling artifacts.

5.2. Further improvements based on automatic outlier removal

In last section, we know that in order to achieve better reconstruction results, it is better to reject these imperfect segments and only use the remainder compatible intensity measurement for FPM reconstruction. Thus, the second strategy is developed to automatically detect and omit those imperfect segments to maintain the consistency of FPM dataset and to bypass or alleviate the vignetting-induced reconstruction artifacts. Comparing those BF images or DF images in both LSI with LSV models, the differences are not huge in the small segments, but the imperfect segments will have distinct intensity differences. The LSV model can help us to automatically detect those images rather than human in-

tervention by setting a threshold value to the difference of LSI and LSV model as follows.

$$I_{i,LSV} - I_{i,LSI} \geq 0.1 \quad (12)$$

The datasets have been preprocessed and normalized [29]. We further found that the performance of the automatic outlier removal strategy is not quite sensitive to the choice the threshold. Because the differences between the BF and DF images are significant [26]. A reasonably good result can always be obtained by fixing the threshold to 0.1, which makes our approach nonparametric and very easy to use in practical applications. Compared with the method to compare the simulated patterns in LSI model with the captured segments, our method will be more precise in selecting those imperfect segments, since both models are simulated models and there is no disturbance of the noise and stay light, and the sequence number of the imperfect segments can be obtained before the FPM reconstruction procedure when the patches have been divided, which will be much helpful for the GPU acceleration of FPM. Therefore, two segments marked in red boxes as shown in Fig. 6(d) are selected with our second strategy, which will be skipped during the update procedure. The reconstructions with our two countermeasures are shown in Fig. 6(b2). Compared with Fig. 6(b1), the artifacts are removed and the Fourier spectrum distribution returns to normal compared with Fig. 6(a).

In addition, we also tested our method in biological samples with our experimentally captured data (rabbit tongue section) and the open-source data (dog stomach cardiac region samples) of Tian et al. [31] for cross validation, as shown in Fig. 7 and Fig. 8 respectively. The system parameters of our data are the same with former experiments. The FOV of rabbit tongue section captured by a $4 \times / 0.1\text{NA}$ objective and one of its small patches (200×200 pixels) far from the center FOV are shown in Fig. 7(a) and (a1), respectively. While the FOV of dog stomach cardiac region sample captured by a $4 \times / 0.1\text{NA}$ objective and a $2 \times$ relay lens and one of its small patches (200×200 pixels) far from the center FOV are shown in Fig. 8(a) and (a1), respectively. The phase information is more important for the biological samples and the phase reconstructions are shown Fig. 7(b1) and Fig. 8(b1) with only the block processing, and obvious artifacts can be observed. But with our second strategy, the segments marked in red boxes in Fig. 7(c) and Fig. 8(c) are selected and

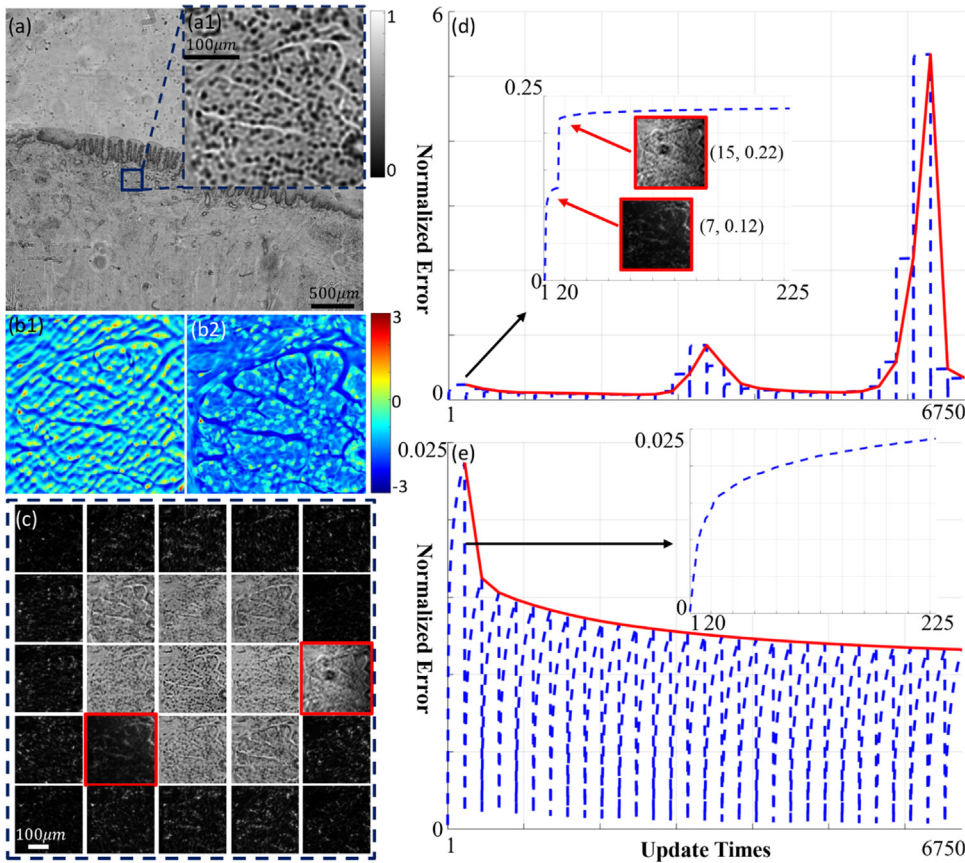


Fig. 7. (a,a1) The FOV of rabbit tongue section captured by a 4×/0.1NA objective and one of its small patches (200 × 200 pixels) and its close-up. (b1,b2) The phase reconstructions with and without automatic outlier removal respectively; (a1,b1,b2) share the same scale bar of 100 µm. (c) The small segments and automatically selected segments to be omitted (red boxes). (d,e) The error matrix with or without automatic outlier removal respectively. Red line, error curves with iterations; blue line, error curves with sub-iterations for each segment. A full iteration contains 255 updates (sub-iterations).

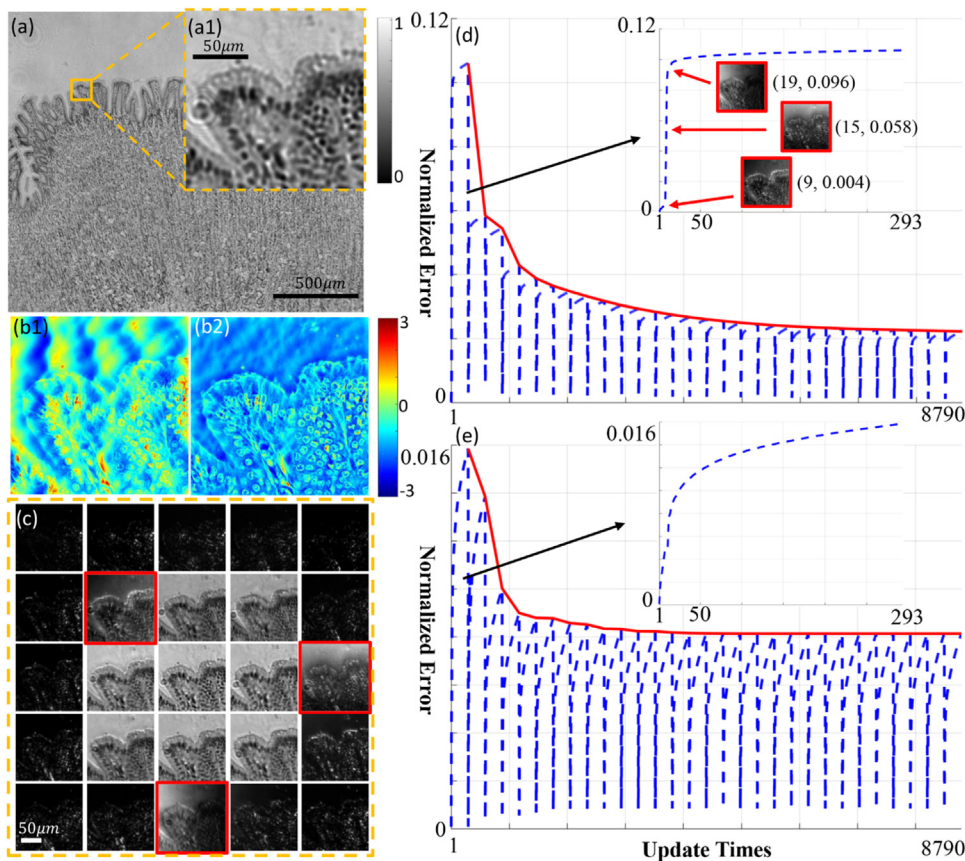


Fig. 8. (a,a1) The FOV of dog stomach cardiac region sample captured by a 4×/0.1NA objective and a 2× relay lens and one of its small patches (200 × 200 pixels) and its close-up [31]. (b1,b2) The phase reconstructions with and without automatic outlier removal respectively; (a1,b1,b2) share the same scale bar of 100 µm. (c) The small segments and automatically selected segments to be omitted (red boxes). (d,e) The error matrix with or without automatic outlier removal respectively. Red line, error curves with iterations; blue line, error curves with sub-iterations for each segment. A full iteration contains 293 updates (sub-iterations).

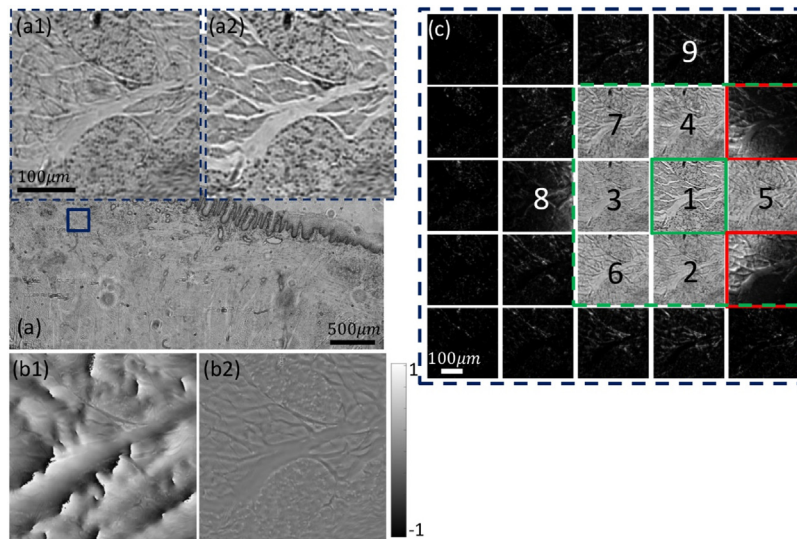


Fig. 9. (a,a1,a2) The FOV of rabbit tongue section captured by a $4\times/0.1\text{NA}$ objective and one of its small patches (200×200 pixels) and its close-ups as the initial guess with the normal incidence and adjacent incidence respectively. (b1,b2) The phase reconstructions with and without our method respectively. (a1,a2,b1,b2) share the same scale bar of $100\mu\text{m}$. (c) The corresponding small segments. Red boxes, segments to be deserted; Green solid box, new initial guess and its close-up, Fig. 9(a2); Green dashed box, BF segments; Sequence number, partial new update order.

omitted automatically. And the reconstructions are shown in Fig. 7(b2) and Fig. 8(b2) respectively, which are improved. To evaluate the image quality, the error matrix with or without automatic outlier removal are shown in Fig. 7(d) and (e), Figs. 8(d) and (e) respectively. The error in the subgraph of Fig. 7(d) is 10 times higher than our methods in Fig. 7(e) after the first iteration and will be enlarged with more iterations (note the significant difference (0.025 and 6) of the maximum y-coordinate between Fig. 7(d) and (e)). These two imperfect or incompatible segments make the algorithm strongly oscillatory and finally divergent. But after 30 iterations, i.e. 6750 updates (sub-iterations), the error matrix converges to around 0.01 with our methods. While the error in the subgraph of Fig. 8(d) is 7.5 times higher than the our methods in Fig. 8(e) after the first iterations. The error of Fig. 8(e) converges to 0.008 within 30 iterations, i.e. 8790 updates (sub-iterations) since 293 images are collected in Ref.30, which is much lower than the error in Fig. 8(d). It can be concluded that our method can recover the phase of the sample very well and avoid appearing pleated artifacts which are caused by the vignetting.

6. Adaptive update order and initial guess strategy

Generally, the update order is fixed for all the patches from the center segments to the peripheral segments, and the center LR image is usually chosen as the initial guess in the FPM [1–3]. However, there may be a shift for all the BF segments when the patch is near the edge of FOV as shown in Fig. 9, since the normal incidence light for different patches is not always the light from the center LED. The experiment parameters are the same as Fig. 7. The reconstructions become bad as shown in Fig. 9(b1) if we still use the fixed update order and initial guess (Fig. 9(a1)) scheme for this patch. Initial guess as discussed in [4,31] works best from an image acquired during the experiment that closely resembles the final image. So the segment marked in green box should be chosen as the initial guess in this case and its close-up is shown in Fig. 9(a2). Compared both initial guesses, Fig. 9(a2) has better contrast than Fig. 9(a1) and is closer to the final image. And the update order as discussed in [38] works best with the intensity order. So combined with the two previous countermeasures, we propose an adaptive update order and initial guess strategy. First, we select out those BF segments (green dashed box in Fig. 9(c)) whose illumination NAs (NA_{illu}) are lower than the objective NA (NA_{obj}) and set the segments with the lowest NA_{illu} as the initial guess (green solid box). Second, we sort the segments except for those deserted segments with the intensity from high to low as the update order (sequence number in Fig. 9(c)) and all the BF segments

should be updated firstly before the DF segments. The reconstructions are improved with our strategy as shown in Fig. 9(b2). It can be concluded that our method can recover the sample very well, especially those patches at the edge of FOV.

7. Conclusions and discussions

Our analysis shows that for a practical FPM microscope with a low magnification objective and a large FOV, the LSI model is destroyed as a result of diffraction at other stops or apertures associated with different lens elements. A modified version of the LSV model is derived for quantitative analysis. The spectrum of the object will be modulated unexpectedly by a quadratic phase term if assuming the shape of pupil function is invariable. However, directly using the LSV model for the reconstructions of FPM is difficult and even impossible. Therefore, two countermeasures are also presented and verified to bypass or alleviate the vignetting-induced reconstruction artifacts. An adaptive update order and initial guess strategy is proposed and demonstrated. So far, the main error sources in FPM come from five parts, i.e. aberrations, LED brightness fluctuations, LED positional misalignments, noise and vignetting effect, all of which may severely degrade the reconstruction results with similar artifacts unexpectedly despite the different generation mechanisms. Even the systematic error is generally a mixture of various error sources in the real situation. The conflict of different advanced algorithm for different error sources have been revealed by Pan [25]. But fortunately, our countermeasures for vignetting can be directly combined with other state-of-art algorithms, since the most important contribution of our strategies for FPM is to seek out those imperfect segments exactly and beforehand, and to degenerate the LSV model to LSI model for other methods to combine freely.

Finally, it should be mentioned that in this work, we are mainly focusing on imaging absorbent samples in which the effect of phase component can be neglected. Benefiting from the inherent data redundancy of FPM, the amplitude information in the missing spectrum regions corresponding to the omitted intensity segments can be automatically filled by other adjacent intensity segments. However, when the sample contains strong phase effect, these “semi-bright and semi-dark” images located at the edge of the NA of objective contains the crucial low-frequency phase information which cannot be supplied by other images [8]. Thus, simply omitting these imperfect images may result in inaccurate phase reconstructions, which may not be the optimal solution. Thus, how to handle the vignetting effect for both cases (amplitude and phase imaging) is an interesting direction for further investigation.

Disclosures

The authors have no relevant financial interests in this article and no potential conflicts of interest to disclose.

Acknowledgments

B. Yao thanks the funds from National Natural Science Foundation of China (NSFC) (81427802 and 61377008). C. Zuo thanks the funds from NSFC (61722506; 61505081 and 11574152), and Outstanding Youth Foundation of Jiangsu Province of China (BK20170034). An Pan thanks Dr. Maosen Li (Xidian University, China) for the valuable and helpful discussions.

Supplementary materials

Supplementary material associated with this article can be found, in the online version, at [doi:10.1016/j.optlaseng.2019.02.015](https://doi.org/10.1016/j.optlaseng.2019.02.015).

References

- [1] Zheng G, Horstmeyer R, Yang C. Wide-field, high-resolution Fourier Ptychographic microscopy. *Nat Photon* 2013;7(9):739–45.
- [2] Ou X, Horstmeyer R, Yang C, Zheng G. Quantitative phase imaging via Fourier Ptychographic microscopy. *Opt Lett* 2013;38(22):4845–8.
- [3] Ou X, Horstmeyer R, Zheng G, Yang C. High numerical aperture Fourier Ptychography: principle, implementation and characterization. *Opt Express* 2015;23(3):3472–91.
- [4] Tian L, Liu Z, Yeh L, Chen M, Zhong J, Waller L. Computational illumination for high-speed in vitro Fourier Ptychographic microscopy. *Optica* 2015;2(10):904–11.
- [5] Pan A, Zhang Y, Wen K, Zhou M, Min J, Lei M, Yao B. Subwavelength resolution Fourier Ptychography with hemispherical digital condensers. *Opt Express* 2018;26(18):23119–31.
- [6] Horstmeyer R, Chung J, Ou X, Zheng G, Yang C. Diffraction tomography with Fourier Ptychography. *Optica* 2016;3(8):827–35.
- [7] Sun J, Zuo C, Zhang L, Chen Q. Resolution-enhanced Fourier Ptychographic microscopy based on high-numerical-aperture illuminations. *Sci Rep* 2017;7:1187.
- [8] Sun J, Zuo C, Zhang J, Fan Y, Chen Q. High-speed Fourier Ptychographic microscopy based on programmable annular illuminations. *Sci Rep* 2018;8:7669.
- [9] Pacheco S, Zheng G, Liang R. Reflective Fourier Ptychography. *J Biomed Opt* 2016;21(2):026010.
- [10] Rodenburg JM, Faulkner HML. A phase retrieval algorithm for shifting illumination. *Appl Phys Lett* 2004;85(20):4795–7.
- [11] Maiden AM, Rodenburg JM. An improved Ptychographical phase retrieval algorithm for diffractive imaging. *Ultramicroscopy* 2009;109(10):1256–62.
- [12] Mico V, Zalevsky Z, Garcia-Martinez P, Garcia J. Synthetic aperture superresolution with multiple offaxis holograms. *J Opt Soc Am A* 2006;23(12):3162–70.
- [13] Tippie AE, Kumar A, Fienup JR. High-resolution synthetic-aperture digital holography with digital phase and pupil correction. *Opt Express* 2011;19(13):12027–38.
- [14] Gustafsson MG, Shao L, Carlton PM, Wang CJ, Golubovskaya IN, Cande WZ, Agard DA, Sedat JW. Three-dimensional resolution doubling in wide-field fluorescence microscopy by structured illumination. *Biophys J* 2008;94(12):4957–70.
- [15] Dan D, Lei M, Yao B, Wang W, Winterhalder M, Zumbusch A, Qi Y, Xia L, Yan S, Yang Y, Gao P, Ye T, Zhao W. DMD-based LED-illumination super-resolution and optical sectioning microscopy. *Sci Rep* 2013;3:1116.
- [16] Horstmeyer R, Ou X, Zheng G, Willems P, Yang C. Digital pathology with Fourier Ptychography. *Comput Med Imag Grap* 2015;42:38–43.
- [17] Guo K, Liao J, Bian Z, Heng X, Zheng G. InstantScope: a low-cost whole slide imaging system with instant focal plane detection. *Biomed Opt Express* 2015;6(9):3210–16.
- [18] Dong S, Nanda P, Shiradkar R, Guo K, Zheng G. High-resolution fluorescence imaging via pattern-illuminated Fourier Ptychography. *Opt Express* 2014;22(17):20856–70.
- [19] Chung J, Kim J, Ou X, Horstmeyer R, Yang C. Wide field-of-view fluorescence image deconvolution with aberration-estimation from Fourier Ptychography. *Biomed Opt Express* 2016;7(2):352–68.
- [20] Goodman JW. Introduction to Fourier optics. Roberts and Company Publishers; 2004.
- [21] Horstmeyer R, Heintzmann R, Popescu G, Waller L, Yang C. Standardizing the resolution claims for coherent microscopy. *Nat Photon* 2016;10:68–76.
- [22] Ou X, Zheng G, Yang C. Embedded pupil function recovery for Fourier Ptychographic microscopy. *Opt Express* 2014;22(5):4960–72.
- [23] Bian Z, Dong S, Zheng G. Adaptive system correction for robust Fourier Ptychographic imaging. *Opt Express* 2013;21(26):32400–10.
- [24] Sun J, Chen Q, Zhang Y, Zuo C. Efficient positional misalignment correction method for Fourier Ptychographic microscopy. *Biomed Opt Express* 2016;7(3):1336–50.
- [25] Pan A, Zhang Y, Zhao T, Wang Z, Dan D, Lei M, Yao B. System calibration method for Fourier Ptychographic microscopy. *J Biomed Opt* 2017;22(9):096005.
- [26] Zuo C, Sun J, Chen Q. Adaptive step-size strategy for noise-robust Fourier Ptychographic microscopy. *Opt Express* 2016;24(18):20724–44.
- [27] Yeh L-H, Dong J, Zhong J, Tian L, Chen M, Tang G, Soltanolkotabi M, Waller L. Experimental robustness of Fourier Ptychography phase retrieval algorithms. *Opt Express* 2015;23(26):33214–40.
- [28] Bian L, Zheng G, Guo K, Suo J, Yang C, Chen F, Dai Q. Motion-corrected Fourier Ptychography. *Biomed Opt Express* 2016;7(11):4543–53.
- [29] Zhang Y, Pan A, Lei M, Yao B. Data preprocessing methods for robust Fourier Ptychographic microscopy. *Opt Eng* 2017;56(12):123107.
- [30] Fan Y, Sun J, Chen Q, Wang M, Zuo C. Adaptive denoising method for Fourier Ptychographic microscopy. *Opt Commun* 2017;404:23–31.
- [31] Tian L, Li X, Ramchandran K, Waller L. Multiplexed coded illumination for Fourier Ptychography with an LED array microscope. *Biomed Opt Express* 2014;5(7):2376–89.
- [32] Wang Z, Lei M, Yao B, Cai Y, Liang Y, Yang Y, Yang X, Li H, Xiong D. Compact multi-band fluorescent microscope with an electrically tunable lens for autofocusing. *Biomed Opt Express* 2015;6(11):4353–64.
- [33] Rayleigh L. On the theory of optical images, with special references to the microscope. *Phil Mag* 1896;42(5):167.
- [34] Kelly DP, Sheridan JT, Rhodes WT. Fundamental diffraction limitations in a paraxial 4-f imaging system with coherent and incoherent illumination. *J Opt Soc Am A* 2007;24(7):1911–19.
- [35] Tichenor DA, Goodman JM. Coherent transfer function. *J Opt Soc Am* 1972;62(2):293–5.
- [36] Zuo C, Chen Q, Qu W, Asundi A. Phase aberration compensation in digital holographic microscopy based on principal component analysis. *Opt Lett* 2013;38(10):1724–5.
- [37] Gibbs JW. Fourier series. *Nature* 1898;59:200.
- [38] Guo K, Dong S, Nanda P, Zheng G. Optimization of sampling pattern and the design of Fourier Ptychographic illuminator. *Opt Express* 2015;23(5):6171–80.